# Temperature Correction and Reflection Removal in Thermal Images using 3D Temperature Mapping

Björn Zeise and Bernardo Wagner
*Institute of Systems Engineering, Real Time Systems Group, Leibniz Universität Hannover, Appelstr. 9A, D-30167, Hannover, Germany*

Keywords: Infrared Thermography, 3D Temperature Mapping, Emissivity Estimation, Temperature Correction, Thermal Reflection Removal, Mobile Service Robotics.

Abstract: Many mobile robots nowadays use thermal imaging cameras (TICs) in order to enhance the environment model that is created during exploration tasks. In conventional thermography, thermal images always have to be carefully revised by human operators, which is not practicable in autonomous applications. Unknown surface emissivities are the main source of misinterpretations in thermal images. In this work, we present two methods dealing with these misinterpretations by exploiting the TIC's changing point of view. While the first approach classifies the regarded material in order to estimate improved surface temperature values, the second one is capable of detecting and removing thermal reflections. The spatial relationship between the thermal images and the regarded surface is made by using a rigidly mounted sensor stack consisting of a TIC and a 3D laser range finder, whose extrinsic calibration is described. During evaluation, we demonstrate the functionality of both approaches.

## 1 INTRODUCTION

In the domain of mobile service robotics, there are plenty of possible use cases for thermal imaging cameras (TICs) – not only in the context of search and rescue (Aziz and Mertsching, 2010), but also for inspection tasks (Vidas et al., 2013) or traffic surveillance (Iwasaki et al., 2013). Connecting 2D thermal images with 3D structural information brings benefits to robotic applications, e.g. when robot operators have to make quick decisions in demanding situations or in the context of self preservation regarding an autonomously acting robot. The projection of thermal images onto 3D structures is called temperature mapping and depicts one of the topics covered in this work.

While the general procedure of temperature mapping is similar to RGB mapping, there are possible sources of misinterpretations in thermal images influencing the temperature mapping results. This work focuses on two of them, namely the temperature misinterpretations arising from unknown emissivity values as well as from thermal reflections (see Figure 1). While a human operator would probably have no problems figuring out that the thermal image shows reflections or incorrectly interpreted temperature values on metal surfaces, this is a rather hard task for a robot. Misinterpreted environment information can lead to false assessment of the current situation which in turn can endanger the accomplishment of the whole mission.

This work brings the following contributions to the domain of thermography in mobile robotics: First, we describe how to calibrate a TIC and a 3D laser range finder (LRF) using a heated calibration trihedron. We estimate the extrinsic calibration parameters in order to provide 3D points measured by the LRF with temperature information. The second contribution is an extension of our previous work (Zeise et al., 2015) aiming at improving temperature measurements of dielectric and metal surfaces. Using the robot's capability of changing its point of view, we exploit the emissivity's viewing angle dependency in order to classify the surface material and correct the measured temperatures accordingly. In contrast to our previous work, this is performed not only for individual surface points and lines, but also for 2D images of a mixed-material surface. The third contribution is an algorithm that identifies and eliminates moving thermal reflections.

The remainder of the paper is organized as follows: In Section 2, we give an overview on related



Zeise, B. and Wagner, B.
Temperature Correction and Reflection Removal in Thermal Images using 3D Temperature Mapping.
DOI: 10.5220/0005955801580165
In *Proceedings of the 13th International Conference on Informatics in Control, Automation and Robotics (ICINCO 2016) - Volume 2*, pages 158-165
ISBN: 978-989-758-198-4

(a) Thermal image (b) RGB image

Figure 1: Exemplary thermal reflection: (a) False-colored thermal image of a person containing a highly reflective metal surface which reflects the person's thermal radiation and (b) a RGB image of the same scene.

work. In Section 3, we describe how to find the extrinsic calibration parameters needed to perform temperature mapping. Section 4 explains our approaches to correcting temperatures and removing reflections from thermal images. We close with an evaluation of the proposed methods in Section 5, concluding the presented work in Section 6.

## 2 RELATED WORK

Finding the extrinsic calibration parameters of a LRF and a camera has been investigated in several works. In (Zhang and Pless, 2004), the extrinsic calibration of a camera and a 2D LRF is described. After finding initial guesses for intrinsic and extrinsic parameters with the help of a planar checkerboard pattern, the calibration result is further refined using non-linear minimization. Regarding the calibration between a 3D LRF and a camera, a similar procedure was used in works such as (Pandey et al., 2010) and (Gong et al., 2013). In these approaches, planes are detected in both the laser and camera observations to determine the transformation between the sensor frames.

Temperature mapping is a well-known problem not only in the robotics domain. The most common method is to use a ray tracing algorithm, that calculates the intersections of the laser rays and the camera image plane. This principle has been applied by e.g. (Alba et al., 2011), (Borrmann et al., 2013) and (Vidas et al., 2013) with different kinds of range sensors.

The effect of a TIC's varying viewing angle has been investigated in (Litwa, 2010) and (Muniz et al., 2014) for dielectrics, and in (Iuchi and Furukawa, 2004) for metals. In (Zeise et al., 2015), we recently showed an approach to reducing misinterpretations in thermal images resulting from unknown emissivity values. For this purpose, we exploited the different emissivity characteristics of dielectrics and metals. Using the TIC's viewing angle we were able to improve the interpretation of temperature values of low-emissivity surface points and lines.

The removal of thermal reflections can be achieved either hardware or software-based. A hardware-based solution suppressing thermal reflections with the help of an infrared polarizing filter was presented in (Vollmer et al., 2004). This approach showed partially good result, but also many limitations (expensive infrared polarizing filter; compliance to strict spatial measurement setup). The general principle of most software-based methods is to extract background and foreground layers from the image. This relies on the assumption that the input image is a linear superposition of an object layer and one or more reflection layers. In (Planas-Cuchi et al., 2003), a user-assisted, single-image approach is presented. Several authors make use of multiple images of the same scene taken with different camera configurations. Varying the polarizer setting (Farid and Adelson, 1999), changing the focus (Schechner et al., 2000) or applying flashlight (Agrawal et al., 2005) allows to separate the layers. In order to use these methods, two still images of the same scene have to be taken, which is not always possible on a mobile robot. The reflection handling method most relevant to our work is the use of the camera's changing point of view. Approaches to this have been presented in (Criminisi et al., 2005), (Li and Brown, 2013) and (Szeliski et al., 2000).

## 3 EXTRINSIC LASER-CAMERA CALIBRATION

The main challenge of temperature mapping lies in proper geometric calibration of the sensors. The LRF[1] and the TIC are mounted in a rigid setup, that can be seen in Figure 2(a). Pointing the sensor stack at a calibration target of known dimensions, we first find the transformations between the individual sensors and the calibration target. After that, the transformations between the sensor coordinate frames (i.e. the TIC's and the LRF's coordinate frames) can be calculated. Since we focus on finding the extrinsic calibration parameters of the sensors, we assume the intrinsic calibration parameters for both sensors to be known.

Since the calibration procedure is mainly based on the approach of (Gong et al., 2013), we only give

[1]By using the term LRF, we mean a 3D LRF unless otherwise indicated.

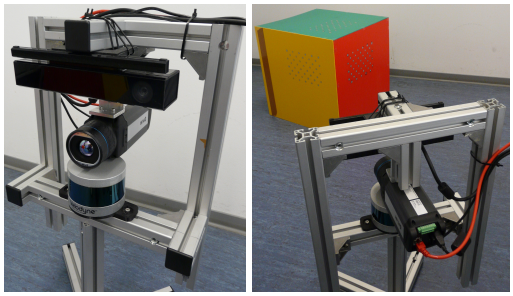

(a) Sensor stack (b) Calibration setup

Figure 2: Sensors used during calibration: (a) sensor setup consisting of LRF (bottom), TIC (center) and Kinect v2 (top, not used in this work), and (b) calibration setup between the sensor stack and the calibration target.

a short explanation at this place. The general calibration setup is depicted in Figure 2(b). Let us define different coordinate frames $(X,Y,Z)$ by using the indices $c$, $l$ and $t$ in order to express quantities with respect to the camera, laser and trihedron coordinate systems (see also Figure 3). The extrinsic calibration between the LRF and the TIC is defined by a $(3 \times 3)$ rotation matrix $\mathbf{R}_{lc}$ and a $(3 \times 1)$ translation vector $\mathbf{t}_{lc}$. This transformation can also be expressed as a transformation from the laser coordinate frame to the trihedron coordinate frame $(\mathbf{R}_{lt},\mathbf{t}_{lt}) = (\mathbf{R}_{tl}^{-1},\mathbf{t}_{tl}^{-1})$, followed by a transformation to the camera coordinate frame $(\mathbf{R}_{tc},\mathbf{t}_{tc})$. A 3D point $\mathbf{p}_l$ with respect to the laser coordinate frame can be projected onto the TIC's image plane using the pinhole camera model:

$$s \begin{bmatrix} u \\ v \\ 1 \end{bmatrix} = \mathbf{K}\left(\mathbf{R}_{lc}\mathbf{p}_l + \mathbf{t}_{lc}\right), \qquad (1)$$

where $[u\ v]^T$ is a 2D point in the image plane scaled by the factor $s$ and $\mathbf{K}$ is the camera matrix containing intrinsic calibration parameters.

In order to find the individual geometric transformations, a common calibration target is needed. We use a heated trihedron whose planes made of PVC are orthogonally oriented. On each of these planes, a pattern of small circles was created using aluminum-containing spray. Observing these three planes with the LRF allows to find the transformation from the trihedron coordinate frame to the laser coordinate frame $(\mathbf{R}_{tl},\mathbf{t}_{tl})$. In the thermal image, the circles of the patterns let us find the corresponding transformation from the trihedron coordinate frame to the camera coordinate frame $(\mathbf{R}_{tc},\mathbf{t}_{tc})$.

In the following subsections, we show how to find the initial transformations for the optimization procedure and how to refine the calibration parameters.

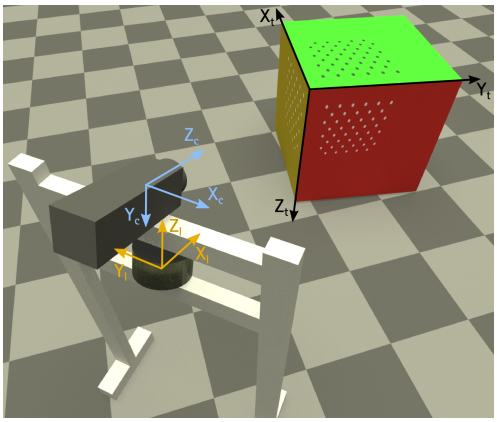


Figure 3: Model of the calibration setup: Coordinate frames of the TIC $(X_c,Y_c,Z_c)$, of the LRF $(X_l,Y_l,Z_l)$ as well as of the calibration trihedron $(X_t,Y_t,Z_t)$. On each plane of the trihedron, there is a pattern consisting of small circles.

## 3.1 Finding Initial Transformations

Finding the rotation matrix $\mathbf{R}_{tl}$ and translation vector $\mathbf{t}_{tl}$ that transform 3D points with respect to the trihedron coordinate frame to 3D points with respect to the laser coordinate frame is accomplished using the plane equations for each of the trihedron's planes. In the following explanations, we utilize a superscript notation using $i$, $j$ and $k$ (or variations) to refer to individual laser-camera data pairs $(i \in 1,2,...,I)$, individual planes $(j \in 1,2,3)$ and individual 3D points $(k \in 1,2,...,K)$ lying in a plane. The plane equations are acquired with the help of a RANSAC-based plane extraction method. Each of the planes detected by the LRF is defined by a unit normal vector $\hat{\mathbf{n}}_l^{(j)}$ and a distance $d_l^{(j)}$ from the laser coordinate frame's origin to the plane. The corresponding plane equation is $\mathbf{p}_l^{(j)}\hat{\mathbf{n}}_l^{(j)} - d_l^{(j)} = 0$, where $\mathbf{p}_l^{(j)}$ is an arbitrary point lying in the $j$th plane.

The individual columns of $\mathbf{R}_{tl}$ depict the planes' unit normal vectors $\hat{\mathbf{n}}_l^{(j)}$ with the result that:

$$\mathbf{R}_{tl} = \begin{bmatrix} \hat{n}_{l,x}^{(1)} & \hat{n}_{l,x}^{(2)} & \hat{n}_{l,x}^{(3)} \\ \hat{n}_{l,y}^{(1)} & \hat{n}_{l,y}^{(2)} & \hat{n}_{l,y}^{(3)} \\ \hat{n}_{l,z}^{(1)} & \hat{n}_{l,z}^{(2)} & \hat{n}_{l,z}^{(3)} \end{bmatrix}. \qquad (2)$$

The translation vector $\mathbf{t}_{tl}$ can be calculated multiplying $\mathbf{R}_{tl}$ with the vector of plane distances:

$$\mathbf{t}_{tl} = \mathbf{R}_{tl} \begin{bmatrix} d_l^{(1)} \\ d_l^{(2)} \\ d_l^{(3)} \end{bmatrix}. \qquad (3)$$

This vector points from the laser coordinate frame's origin to the trihedron's corner, which is also the origin of the trihedron coordinate frame.

The determination of rotation matrix $\mathbf{R}_{tc}$ and translation vector $\mathbf{t}_{tc}$ that transform 3D points with respect to the trihedron coordinate frame to 3D points with respect to the camera coordinate frame is quite similar to the procedure described above. Using the circle grid patterns, we find the rotation matrices and translation vectors for transforming the individual pattern coordinate frames to the camera coordinate frame. These matrices and vectors can then be related to the trihedron coordinate frame. The columns of $\mathbf{R}_{tc}$, just like for the laser transformation, are the planes' unit normal vectors, i.e. the third column $\mathbf{r}_3^{(j)}$ of the rotation matrix found for each pattern/plane $j \in \{1,2,3\}$:

$$\mathbf{R}_{tc} = \begin{bmatrix} \mathbf{r}_3^{(1)} & \mathbf{r}_3^{(2)} & \mathbf{r}_3^{(3)} \end{bmatrix}. \tag{4}$$

The translation vector $\mathbf{t}_{tc}$ that points from the camera coordinate frame's origin to the trihedron's origin can be calculated with the help of one of the pattern-camera transformations by shifting the pattern's origin to the trihedron's origin.

### 3.2 Refining Calibration Parameters

A refinement of the calibration parameters can be accomplished by matching the laser points lying in the trihedron's planes into the plane equations estimated based on the thermal image data. Hence, we try to find $\mathbf{R}_{lc}$ and $\mathbf{t}_{lc}$ that satisfy the Hesse normal form of each trihedron's plane. This can be expressed as an optimization problem of the following form:

$$\underset{\mathbf{R}_{lc},\mathbf{t}_{lc}}{\operatorname{argmin}} \sum_{i=1}^{I} \sum_{j=1}^{3} \sum_{k=1}^{K} \left\| \hat{\mathbf{n}}_c^{(i,j)} (\mathbf{R}_{lc} \mathbf{p}_l^{(i,j,k)} + \mathbf{t}_{lc}) - d_c^{(i,j)} \right\|^2, \tag{5}$$

where $K$ is the total number of points detected by the LRF in one specific plane $j$ and data pair $i$, and $I$ is the total number of laser-camera data pairs taken. A solution for this non-linear least squares problem can be found using the Levenberg-Marquardt algorithm.

## 4 HANDLING OF MISINTERPRETATIONS

Most misinterpretations in thermal images originate from an unknown emissivity $\varepsilon$, which is a surface-specific property dependent especially on the type of surface material and the TIC's viewing angle. The viewing angle is the angle between the camera's optical axis and the surface normal of the regarded point. According to (Martiny et al., 1996), the signal measured by the TIC can be expressed as:

$$S_{sum} = \varepsilon S_{obj} + (1-\varepsilon) S_{amb} \tag{6}$$

with

$$S_{obj} = \frac{R}{\exp\left(\frac{B}{T_{obj}}\right) - F} \tag{7}$$

and

$$S_{amb} = \frac{R}{\exp\left(\frac{B}{T_{amb}}\right) - F}, \tag{8}$$

if the the atmospheric amount of radiation power is neglected. In Equation 6, $S_{sum}$, $S_{obj}$ and $S_{amb}$ represent output signals measured per image pixel. According to the subscripts, they depict the total output signal, the output signal corresponding to the regarded object's radiation power and the output signal corresponding to the reflected ambience's radiation power. In Equations 7 and 8, $T_{obj}$ and $T_{amb}$ are the true object/ambient temperatures, while $R$, $B$ and $F$ are camera-specific parameters provided by the TIC's manufacturer. From Equation 6, it can be seen that the higher the emissivity value, the smaller the influence of ambient reflections on the thermal image.

Since in mobile robot exploration a preparation of the environment before measurement (e.g. using high emissivity coatings) is not applicable, we developed two methods for improving the interpretation of thermal images regarding unknown surface emissivities and thermal reflections.

### 4.1 Estimation of Unknown Emissivities

This section refers to our previous work in (Zeise et al., 2015), where we showed the feasibility of temperature correction for surfaces regarded from a known viewing angle. In our approach, we estimated improved surface temperature values of metal and dielectric surface points exploiting the different emissivity characteristics of metals and dielectrics at a varying viewing angle.

In general, the approach divides into two subroutines. The first step is to determine the regarded surface point's material class, i.e. metal or dielectric. This can be done by observing one individual point's output signal at different viewing angles. As we derived from Equation 6, the total output signal depends linearly on the emissivity. Due to the fact that the emissivity in general shows a qualitative behavior as depicted in Figure 4, it is sufficient to investigate the individual pixel's output signal in order to assign one of the properties *metal* or *dielectric* to the point.

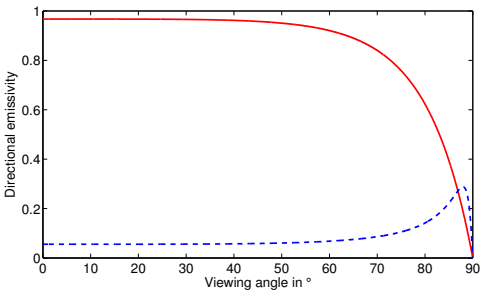


Figure 4: Qualitative comparison of metal (blue, dashed line) and dielectric (red, solid line) emissivity characteristics depending on the viewing angle.

The second step is to estimate improved temperature values for each individual point on the surface. This can be done using non-linear least squares optimization minimizing the error between the measured output signals at different viewing angles and theoretically calculated output signals that depend mostly on emissivity. Equations describing emissivity as a function of the viewing angle can be found in the literature, e.g. in (Howell et al., 2011). The minimization is performed as:

$$\underset{\mathbf{p}}{\operatorname{argmin}} \sum_{z=1}^{Z} \left(S_z^m - S_z^c(\mathbf{p})\right)^2, \qquad (9)$$

where $\mathbf{p} = \{n, k, T_{obj}, T_{amb}\}$ is the set of parameters to be found. In this set of parameters, the refractive index $n$ and the extinction coefficient $k$, together with the corresponding viewing angle, describe the graph of emissivity ε. The signals $S_z^m$ and $S_z^c$ represent measured/calculated values at $Z$ different viewing angles.

In order to use our approach, some assumptions have to be made. On the one hand, both the surface temperature $T_{obj}$ and the ambient temperature $T_{amb}$ are assumed to be unknown but constant. On the other hand, $T_{obj}$ must be higher than $T_{amb}$. Since the assumption that $T_{amb} = const.$ is in conflict with the occurrence of thermal reflections, it is necessary to identify and remove them before correcting the surface temperatures.

## 4.2 Thermal Reflection Removal

Handling of thermal reflections can be accomplished by using background subtraction. The relation of temperature values and 3D information can be used to investigate temperature changes of specific surface points. For our investigations, we assume a static environment, which implies that the temperatures of the regarded surfaces do not change over time. Hence, if an individual surface point's measured temperature does not change when the camera moves, it means

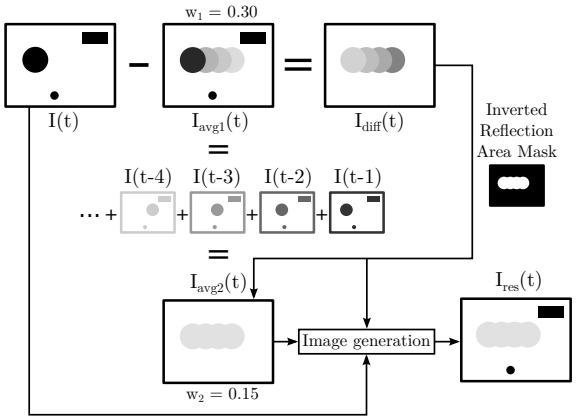


Figure 5: Illustration of the reflection removal procedure: Weighted moving averages of thermal images are used to handle reflections (see the text for a detailed description).

that the temperature is mostly the temperature of the surface itself. In contrast, a changing temperature of one specific surface point implies a superposition of the actual surface temperature and a thermal reflection.

In Figure 5, our approach to thermal reflection removal is illustrated. Let $I(t), I(t-1), ..., I(t-n)$ be a set of registered thermal images of a static scene taken from different points of view. The weighted moving average $I_{avg}(t)$ at time $t$ can be calculated using the following equation:

$$I_{avg}(t) = wI(t) + (1-w)I_{avg}(t-1), \qquad (10)$$

where $w$ is a weighting factor influencing the importance of the latest image $I(t)$. A high value of $w$ means more influence of the current image on the moving average. We use this factor to create two individual moving averages: In the first, $I_{avg1}(t)$, the latest thermal image has a major influence on the average image. Subtracting this average image from the current thermal image gives us $I_{diff}(t)$ that can be regarded as a reflection mask. Every pixel in $I_{diff}(t)$ that is not zero/white represents a potential reflection. The second moving average image, $I_{avg2}(t)$, is created using a smaller weighting factor in combination with the reflection mask. Masking out the non-reflective pixels allows to generate an image that contains only reflective pixels. In contrast to the mask itself and the first average image, the reflective areas in $I_{avg2}(t)$ are very smooth. This smooth image is then used to fill the reflective areas during image generation. Depending on whether the regarded pixel was marked as reflective or not in the reflection mask, the image generation either uses data from $I_{avg2}(t)$ or from $I(t)$ to generate the resulting image $I_{res}(t)$.

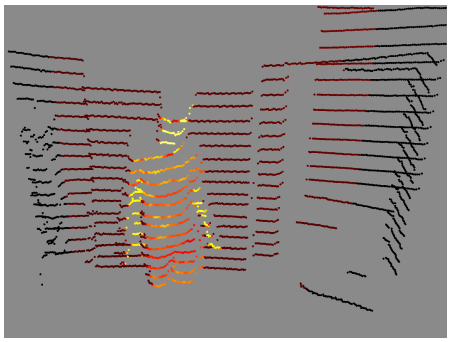

Figure 6: Mapping results: False-colored point cloud showing a person standing in front of a cupboard.

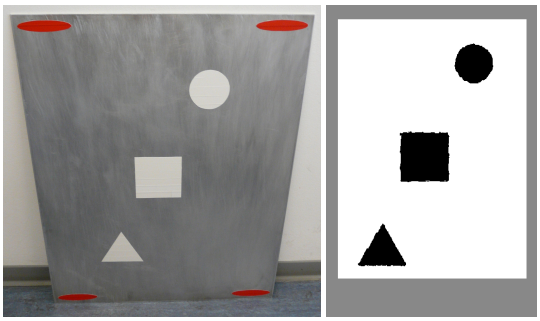

(a) Reflective plate (b) Material classification result

Figure 7: Reflective plate: (a) RGB image of the low-emissive aluminum plate and (b) the result of the material classification procedure (white areas = *metal*, black areas = *dielectric*, gray areas = not specified).

## 5 EVALUATION

The evaluation was performed using the *Velodyne Puck* LRF and the *Flir A655sc* TIC. The LRF provides dense, horizontal scans with a field of view of 360 °, while the vertical field of view is only 30 ° consisting of 16 scan lines. The TIC has a spatial resolution of 640 x 480 pixels, working in a spectral range between 7.5 $\mu m$ and 14 $\mu m$. The camera's field of view is 45 ° x 34 °.

### 5.1 Laser-Camera Calibration and Temperature Mapping

As stated in Section 3, the intrinsic calibration parameters for the LRF were taken as provided by the manufacturer. The intrinsics of the TIC were estimated using a heated aluminum plate covered with squares made of aluminum and PVC. The parameter estimation was performed using standard computer vision algorithms (Zhang, 2000).

The laser-camera calibration can be assessed looking at the temperature mapping results (Figure 6). Since the vertically sparse point cloud complicates an objective temperature mapping evaluation, we do not provide information on the reprojection error.

### 5.2 Temperature Correction

The temperature correction algorithm was evaluated using the heated, low-emissive aluminum plate (56 *cm* x 70 *cm*) depicted in Figure 7(a). On the plate, there are several stripes of high-emissive duct tape forming shapes of a triangle, a square and a circle. The aim of this evaluation is to first identify the regarded material class for every individual pixel in the thermal image. After that, we use this information to estimate improved values of the surface points' temperatures.

We took more than 50 laser-camera data pairs of the heated plate while continuously increasing the sensors' viewing angle. Using the four elliptic tags near the corners of the plate, we were able to register consecutive images. In addition, we used the LRF's 3D point cloud data to calculate every individual pixel's viewing angle.

The results of the material classification are depicted in Figure 7(b). The algorithm distinguishes between metal and dielectric points by adding up the differences between consecutive measurements taken from increasing viewing angles. If the resulting value is greater than zero, the algorithm tags the surface point as *metal*, otherwise as *dielectric*.

The temperature correction is performed for every individual surface point. Depending on the material class, parameters $n$, $k$, $T_{obj}$ and $T_{amb}$ are estimated using non-linear optimization. To solve the least squares minimization problem, we make use of the Levenberg-Marquardt algorithm.

The plate's true surface temperature was determined using an additional surface thermometer. On the metal areas, we measured a temperature of about 317 $K$. The dielectric shapes had a slightly lower temperature of about 316 $K$. The direction of reflection was covered with a wall having a temperature of about 295 $K$, ensuring a constant ambient temperature $T_{amb}$.

The optimization results are depicted in Figure 8. The aluminum temperatures in the original thermal image are obviously misinterpreted. While in the original image (i.e. without taking emissivity into account) the metal surface had an average temperature of about 297 $K$, our method was able to correct this value to about 305 $K$ for most of the metal sur-

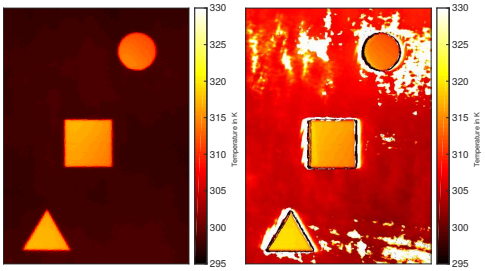


(a) Original thermal image (b) Processed thermal image

Figure 8: Temperature correction results (false-colored): (a) Original thermal image with metal areas interpreted as too cold (dark) and (b) the corrected image with improved temperature interpretations.

face points. Due to a high emissivity of the dielectric points, there are almost no misinterpretations in these areas. Hence, the corrected dielectric temperatures are nearly the same as the ones originally measured.

While in the border areas between dielectric and metal points we expected wrong estimations, the results regarding the metal areas are in need of improvement. This can mostly be traced back to the wavelength dependency of the optical constants $n$ and $k$ (as introduced in Section 4.1). Since all measurements taken by the TIC take into account the whole wavelength spectrum between 7.5 $\mu m$ and 14 $\mu m$, $n$ and $k$, which can vary at different wavelengths, cannot be unambiguously determined. This is also the reason for erroneously estimated high temperature values represented by the bright areas in Figure 8(b).

### 5.3 Reflection Detection and Removal

To evaluate the capabilities of our reflection removal approach, we used the same aluminum plate as for the temperature correction experiment. As stated before, the bare aluminum surface is highly reflective to thermal radiation. We placed a can filled with hot water (approx. 350 $K$) in the direction of reflection. We created a dataset, taking thermal images while simultaneously changing the camera's point of view. Applying our algorithm to this dataset leads to the results depicted in Figure 9.

The resulting image shows that the thermal reflection could be most widely removed. During our experiments, we noticed a thin, black borderline in the corrected image at the edge of the aluminum plate. We trace this back to the fact that our algorithm cuts out the plate in order to ensure an accurate image registration. Assuming a complete 3D environment model in our future research, these borderlines will not be present anymore.

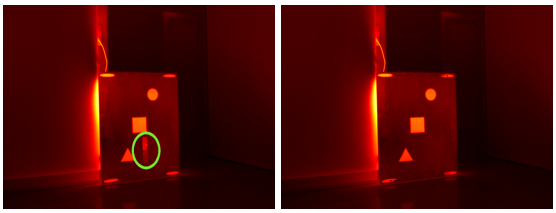

(a) Original image (b) Resulting image

Figure 9: Reflection removal result for an exemplary dataset (false-colored): (a) shows the original image containing a reflection of a can (marked by the ellipse), while (b) depicts the processed image without reflection.

A possible shortcoming of our approach is that only moving reflections can be detected at the moment. For later stages of our work, one solution for this could be to keep track of reflections as soon as they were detected.

## 6 CONCLUSION AND FUTURE WORK

In this work, we faced the problem of handling misinterpretations in thermal images making use of spatial knowledge of the regarded scene. We acquired information of the camera's viewing angle by using a rigidly mounted sensor setup consisting of a TIC and a LRF, which we extrinsically calibrated with the help of a heated calibration trihedron.

We first presented an approach that – using the emissivity's viewing angle dependency – is able to improve temperature measurements of surfaces with unknown emissivity values. Our method showed good results in determining the material class (dielectric/metal) of regarded surface points. While the general functionality of the temperature correction was demonstrated, the results are yet limited due to several unsolved dependencies (e.g. wavelength-dependent optical constants).

The second method presented deals with thermal reflections. Exploiting the TIC's varying viewing angle, our algorithm based on background subtraction was able to detect and remove reflections from the images. Experiments showed that moving thermal reflections could successfully be removed.

Future work will focus on integrating the presented approaches into a 3D simultaneous localization and mapping (SLAM) algorithm. By doing this, our algorithms will benefit from the spatial knowledge of the scene on the one hand, while enhancing the generated environment model with improved temperature mapping on the other hand. Additional effort

can be spent on tuning the performance of the temperature correction algorithm, e.g. by using a GPU implementation.

## ACKNOWLEDGEMENTS

This work has partly been supported within H2020-ICT by the European Commission under grant agreement number 645101 (SmokeBot).

## REFERENCES

Agrawal, A., Raskar, R., Nayar, S. K., and Li, Y. (2005). Removing photography artifacts using gradient projection and flash-exposure sampling. *ACM Trans. Graph.*, 24(3):828–835.

Alba, M. I., Barazzetti, L., Scaioni, M., Rosina, E., and Previtali, M. (2011). Mapping infrared data on terrestrial laser scanning 3D models of buildings. *Remote Sensing*, 3(9):1847–1870.

Aziz, M. Z. and Mertsching, B. (2010). Survivor search with autonomous UGVs using multimodal overt attention. In *IEEE Safety Security and Rescue Robotics*, pages 1–6, Bremen, Germany.

Borrmann, D., Elseberg, J., and Nüchter, A. (2013). Thermal 3D mapping of building façades. In Lee, S., Cho, H., Yoon, K.-J., and Lee, J., editors, *Intelligent Autonomous Systems 12*, number 193 in Advances in Intelligent Systems and Computing, pages 173–182. Springer Berlin Heidelberg, Berlin, Heidelberg.

Criminisi, A., Kang, S. B., Swaminathan, R., Szeliski, R., and Anandan, P. (2005). Extracting layers and analyzing their specular properties using epipolar-plane-image analysis. *Computer Vision and Image Understanding*, 97(1):51–85.

Farid, H. and Adelson, E. H. (1999). Separating reflections and lighting using independent components analysis. In *IEEE Computer Society Conference on Computer Vision and Pattern Recognition*, volume 1, pages 262–267, Fort Collins, CO, USA.

Gong, X., Lin, Y., and Liu, J. (2013). 3D LIDAR-camera extrinsic calibration using an arbitrary trihedron. *Sensors*, 13(2):1902–1918.

Howell, J. R., Siegel, R., and Mengüç, M. P. (2011). *Thermal radiation heat transfer*. CRC Press, Boca Raton, FL, USA, 5th edition.

Iuchi, T. and Furukawa, T. (2004). Some considerations for a method that simultaneously measures the temperature and emissivity of a metal in a high temperature furnace. *Review of Scientific Instruments*, 75(12):5326–5332.

Iwasaki, Y., Kawata, S., and Nakamiya, T. (2013). Vehicle detection even in poor visibility conditions using infrared thermal images and its application to road traffic flow monitoring. In Sobh, T. and Elleithy, K., editors, *Emerging Trends in Computing, Informatics, Systems Sciences, and Engineering*, number 151 in Lecture Notes in Electrical Engineering, pages 997–1009. Springer New York, New York, NY, USA.

Li, Y. and Brown, M. S. (2013). Exploiting reflection change for automatic reflection removal. In *IEEE International Conference on Computer Vision*, pages 2432–2439, Sydney, Australia.

Litwa, M. (2010). Influence of angle of view on temperature measurements using thermovision camera. *IEEE Sensors Journal*, 10(10):1552–1554.

Martiny, M., Schiele, R., Gritsch, M., Schulz, A., and Wittig, S. (1996). In situ calibration for quantitative infrared thermography. In *International Conference on Quantitative InfraRed Thermography*, pages 3–8, Stuttgart, Germany.

Muniz, P. R., Cani, S. P. N., and Magalhães, R. d. S. (2014). Influence of field of view of thermal imagers and angle of view on temperature measurements by infrared thermovision. *IEEE Sensors Journal*, 14(3):729–733.

Pandey, G., McBride, J., Savarese, S., and Eustice, R. (2010). Extrinsic calibration of a 3D laser scanner and an omnidirectional camera. *IFAC Proceedings Volumes*, 43(16):336 – 341.

Planas-Cuchi, E., Chatris, J. M., López, C., and Arnaldos, J. (2003). Determination of flame emissivity in hydrocarbon pool fires using infrared thermography. *Fire Technology*, 39(3):261–273.

Schechner, Y. Y., Kiryati, N., and Basri, R. (2000). Separation of transparent layers using focus. *International Journal of Computer Vision*, 39(1):25–39.

Szeliski, R., Avidan, S., and Anandan, P. (2000). Layer extraction from multiple images containing reflections and transparency. In *IEEE Conference on Computer Vision and Pattern Recognition*, volume 1, pages 246–253, Hilton Head Island, SC, USA.

Vidas, S., Moghadam, P., and Bosse, M. (2013). 3D thermal mapping of building interiors using an RGB-D and thermal camera. In *IEEE International Conference on Robotics and Automation*, pages 2311–2318, Karlsruhe, Germany.

Vollmer, M., Henke, S., Karstädt, D., Möllmann, K. P., and Pinno, F. (2004). Identification and suppression of thermal reflections in infrared thermal imaging. In *InfraMation Proceedings*, volume 5, pages 287–298, Las Vegas, NV, USA.

Zeise, B., Kleinschmidt, S. P., and Wagner, B. (2015). Improving the interpretation of thermal images with the aid of emissivity's angular dependency. In *IEEE International Symposium on Safety, Security, and Rescue Robotics*, pages 1–8, West Lafayette, IN, USA.

Zhang, Q. and Pless, R. (2004). Extrinsic calibration of a camera and laser range finder (improves camera calibration). In *IEEE/RSJ International Conference on Intelligent Robots and Systems*, volume 3, pages 2301–2306, Sendai, Japan.

Zhang, Z. (2000). A flexible new technique for camera calibration. *IEEE Transactions on Pattern Analysis and Machine Intelligence*, 22(11):1330–1334.